Tsunami Debris Damming Forces and Associated Coefficients for Elevated Coastal Structure Columns: Experimental Comparison to ASCE 7-22 Minimum Design Loads

Kellen Doyle[1], Myung-Jin Koh[2], Ravindu Jayasekara[3], Daniel Cox, Ph.D., M.ASCE[4], Hyoungsu Park, Ph.D.[5], Sabarethinam Kameshwar, Ph.D.[6], Pedro Lomonaco, Ph.D.[7]

[1] Graduate Research Assistant, School of Civil and Construction Engineering, Oregon State University, Corvallis, OR 97331; email: doyleke@oregonstate.edu (corresponding author)

[2] PhD Candidate, Department of Civil, Environmental, and Construction Engineering, University of Hawai'i at Manoa, Honolulu, HI, 96822; email: myungj@hawaii.edu

[3] Graduate Student, Department of Civil and Environmental Engineering, Louisiana State University, Baton Rouge, LA, 70803; email: jjayas2@lsu.edu

[4] Professor, School of Civil and Construction Engineering, Oregon State University, Corvallis, OR 97331; email: dan.cox@oregonstate.edu

[5] Assistant Professor, Department of Civil, Environmental, and Construction Engineering, University of Hawai'i at Manoa, Honolulu, HI, 96822; email: hpark9@hawaii.edu

[6] Assistant Professor, Department of Civil and Environmental Engineering, Louisiana State University, Baton Rouge, LA, 70803; email: skameshwar1@lsu.edu

[7] Director, O.H. Hinsdale Wave Research Laboratory, College of Engineering, Oregon State University, Corvallis, OR 97331; email: pedro.lomonaco@oregonstate.edu

ABSTRACT

Debris damming forces of 1:20-scale shipping containers freely accumulated against elevated coastal structure columns were experimentally determined to evaluate ASCE 7-22 tsunami-resilient design standards. Three inundation conditions were generated to represent Froude regimes estimated in post-tsunami field studies. Three different column array densities and two different shipping container sizes were evaluated. A photogrammetric method was employed to estimate the submerged projected area of in-situ transient debris dams from two synchronized camera perspectives. Relative to this experimental data, it was found that the ASCE 7-22 equation for simplified equivalent uniform lateral static pressure (Eq. 2) is conservative by a mean factor of safety of 14.6 and performs as intended given the prescribed scope. Similarly, the ASCE 7-22 equation for detailed hydrodynamic lateral forces (Eq. 3) yielded a lower mean factor of safety of 2.40 but maintained design conservatism across all tested experimental conditions, also performing as intended. Minimum closure ratios and overall structure drag coefficients serve as input values for these detailed hydrodynamic lateral design loads. Proportion of closure coefficients per ASCE 7-22 Sections 6.8.7 and 6.10.2.1 tend to be reasonably conservative in general, and any instances of experimental exceedance of design values did not appear to affect design conservatism of Eq. 3. Finally, drag coefficients for rectilinear structures per ASCE 7-22 Table 6.10-1 appear unrepresentative of elevated coastal structures, which tend to generate column-flow interactions and unbalanced hydrostatic conditions. It is therefore suggested that flow resistance of such structures be quantified via a bulk resistance coefficient, indicated by recent literature as a more appropriate measure applicable to surface-piercing flow obstructions.

PRACTICAL APPLICATIONS

Since the 2016 adoption of tsunami-resilient design standards in ASCE 7-16, debris damming design loads have yet to be thoroughly examined. The results of this experiment indicate that the application of hydrodynamic loading equations in ASCE 7-22 Section 6.10 are conservative across all tested experimental conditions. Debris accumulation on the seaward face of the modeled structure is generally conservative relative to design proportion of closure coefficients and instances of exceedance do not result in unconservative load prediction. Finally, drag coefficients for rectilinear structures may not capture phenomena associated with surface-piercing flow obstructions such as column-flow interactions and unbalanced hydrostatic forces. It is suggested that bulk resistance coefficient be adopted to account for both form drag and surface effects of flow around elevated coastal structure columns. Accurate quantification of tsunami-induced loads is crucial to the design of critical and essential infrastructure located within tsunami inundation zones, especially vertical evacuation refuge structures.

AUTHOR KEYWORDS

Tsunami resilience; debris; column force; closure ratio; drag coefficient; resistance coefficient; vertical evacuation

INTRODUCTION

Tsunami overland flow in coastal areas has the potential to induce widespread debris effects on the built environment, including phases of debris entrainment, transport, impact, and damming. An emphasis on understanding these processes in the context of structural loading and failure modes has grown in recent years following a number of extreme tsunami events (Nistor et al. 2017).

Post-event field studies often highlight the variability of debris types and source locations during coastal inundation. Hurricane Katrina, generating similar damage to that of the 2004 Indian Ocean tsunami, showed that "any floating or mobile object in the nearshore/onshore areas can become floating debris." This event also highlighted the consequences of large debris elements such as shipping containers, boats, barges, and unrestrained storage containers (Robertson et al. 2007).

Following entrainment of debris elements within the inundating flow, debris transport is affected by both the debris itself and the environment through which it moves (Stolle et al. 2020; Park et al. 2021). Debris size, density, and buoyancy have the potential to affect transportation behavior during inundation, while land gradient, built environment density, and inundation depth and velocity affect the likelihood and consequences of debris interaction with structures (Naito et al. 2013).

Debris-structure interaction diverges into impact and damming phenomena. Impact typically induces a short duration peak force as debris strikes the structure or member. Damming typically induces longer duration forces of a lower magnitude that have the potential to slowly yield a structure or member and further accumulate debris. Large debris such as fishing vessels, vehicles, and shipping containers have been observed to cause failure of structural elements, including rigid frames and exterior columns, following both the Indian Ocean tsunami of 2004 and the Japanese tsunami of 2011 (Saatcioglu et al. 2005; Carden et al. 2015).

In response to these and other devastating tsunami events, tsunami-resilient structural design standards were adopted in 2016 in the form of ASCE/SEI 7-16: Minimum Design Loads and Associated Criteria for Buildings and Other Structures (ASCE/SEI 2016). Debris damming considerations in the current edition of these standards, ASCE 7-22 (ASCE/SEI 2022), include two alternative methods of lateral load prediction based in-part on a minimum assumed proportion of closure coefficient due to debris accumulation and an overall structure drag coefficient. These four components are evaluated herein as experimental results are compared to ASCE 7-22 design values.

Laboratory experiments regarding debris damming emerged in the field of hydraulic engineering under steady flow conditions representative of riverine flooding (Bocchiola et al. 2006; Schmocker and Hager 2011; Oudenbroek et al. 2018; Mauti et al. 2020). As of late, unsteady, transient flow conditions in recent laboratory experiments have attempted to better represent coastal inundation events (Stolle et al. 2018; Wütrich et al. 2019; Shekhar et al. 2020). While these studies signal a shift towards tsunami-specific debris damming experiments, most utilized small-scale debris and a limited flume width relative to the structure specimen, which are factors that the experiment presented here aims to improve upon, mainly by minimizing flume wall effects.

Many of these experimental studies note a “surface swell” or unbalanced hydrostatic condition upstream and downstream of a flow obstruction. This presence of a free surface implies that assumptions for quadratic drag – namely a fully-submerged flow obstruction in an infinite fluid field – deteriorate when applied to surface-piercing flow obstructions common in coastal inundation events. As a result, some recent tsunami literature (Stolle et al. 2018; Mauti et al. 2020) has adopted the use of a resistance coefficient (C_r) to capture both form drag and hydrostatic components of flow resistance by a fixed, surface-piercing obstacle. In this study, such a resistance coefficient is explored in contrast to ASCE 7-22 empirical drag coefficients for rectilinear structures.

While extensive research has been performed to understand tsunami debris impact forces, tsunami debris damming remains in need of further research (Nistor et al. 2017). The highly varied, transient nature of tsunami overland flow and the stochastic nature of debris entrainment, transport, and deposition against a coastal structure call for a more thorough understanding of these processes. A thorough examination of current tsunami debris damming load predictions (ASCE/SEI 2022) has yet to be performed. As such, this study aims to:

- assess conservatism of ASCE 7-22 Equations 6.10-1 (Eq. 2) and 6.10-2 (Eq. 3) in quantifying lateral force-resisting system (LFRS) design loads under tsunami-driven debris damming;
- evaluate ASCE 7-22 Section 6.8.7 and 6.10.2.1 design proportion of closure coefficients via a new photogrammetric method to estimate the submerged projected area of ephemeral debris dams under unsteady, transient flow conditions; and
- investigate ASCE 7-22 Table 6.10-1 drag coefficients for rectilinear structures by exploring the application of bulk resistance coefficients to column arrays of elevated coastal structures.

BACKGROUND

Debris Damming Experiments

Many previous debris damming experiments (Bocchiola et al. 2006; Schmocker and Hager 2011; Oudenbroek et al. 2018) investigated large woody debris (LWD) damming in the presence of bridge decks and piers under simulated riverine conditions. Other steady flow experiments employed idealized dam shapes and porosities rather than naturally accumulating LWD elements (Mauti et al. 2020). More exploration must be conducted to examine the application of riverine debris damming findings to tsunami-resilient engineering design (Nistor et al. 2017), specifically with respect to the greater diversity of tsunami-driven debris and the variable structure density of tsunami inundation zones.

A recent shift from steady to unsteady, transient flow has aimed to better represent the conditions surrounding coastal inundation events. Stolle et al. (2018) used a dam-break wave to assess debris damming forces of scaled shipping containers, LWD, and construction materials under supercritical flow conditions. Wütrich et al. (2019) used a vertical-release technique to generate a dry-bed surge in order to quantify LWD and shipping container debris damming forces against a structure of varying porosity. Shekhar et al. (2020) employed an unbroken wave - generated via error function paddle displacement resulting in a single long wave (Bridges et al. 2011) - to investigate impact and damming forces of multiple debris elements against a structure. These studies provide a strong basis for bridging the gap from hydraulic to coastal engineering applications, but often used small-scale debris elements and a limited flume width. A number of these experiments, under both steady (Schmocker and Hager 2011; Mauti et al. 2020) and unsteady flows (Stolle et al. 2018), discussed free-surface elevation increases upstream of a flow obstruction described as a "surface swell," resulting in unbalanced hydrostatic forces.

Resistance Coefficient of Surface-Piercing Flow Obstructions

While ASCE 7-22 provides overall drag coefficients for rectilinear structures, a bulk resistance coefficient commonly seen in hydraulic engineering may be a more suitable measure of flow resistance by an array of surface-piercing obstacles. Drag coefficient traditionally pertains to fully submerged flow obstructions and is used to calculate force on the obstacle due to form drag only. Previous open channel experiments have explored the use of a modified drag coefficient, commonly termed a resistance coefficient, in attempts to capture the more complex hydrodynamics surrounding a surface-piercing flow obstruction.

Chaplin and Teigen (2003) found that loads on a surface-piercing cylinder towed at a steady velocity through a basin of quiescent water were due to both "flow separation and wavemaking," or a form drag component and a free-surface disturbance component. Fenton (2003) and Qi et al. (2014) each explored methods of predicting free-surface increases upstream of a flow obstruction by equating the drag force acting on the obstacle to the change in momentum flux upstream and downstream of the obstacle. While Fenton focused mainly on subcritical flows and noted that some assumptions degraded as flows became transitional, Qi et al. examined mainly choked, supercritical flows that generated hydraulic jumps downstream of the flow obstruction. Both studies retained the use of drag coefficient throughout their derivations which differs from more recent studies, described below.

Recent tsunami-related literature has shown a departure from drag coefficients of surface-piercing obstacles, instead opting to use resistance coefficient as a dimensionless measure of flow resistance. Arnason et al. (2009) described the use of resistance coefficient in transient flow experiments as a method to incorporate free-surface effects due to unbalanced hydrostatic pressure components. Stolle et al. (2018) echoed this, describing resistance coefficient as "a surrogate representing the force from both the form drag and the hydrostatic pressure." Mauti et al. (2020) once again referenced this hydrostatic imbalance, explicitly describing "the change in water depth directly in front of and behind the column." Such descriptions reinforce the earlier observations of Chaplin and Teigen (2003) that flow separation and wavemaking components are not readily separable for hydrodynamic forces. This combination leads to a total resistance force described by a dimensionless resistance coefficient, analogous to a drag force described by a dimensionless drag coefficient.

The use of "bulk" in describing a bulk resistance coefficient is intended to account for interactions between individual columns as they contribute to a resistance coefficient for the entire column array. Rather than quantify blockage (local flow acceleration between flow-perpendicular obstructions) and sheltering (local flow deceleration due to upstream flow obstructions) for each individual column, bulk resistance coefficient captures the net result of all such interferences into a single dimensionless resistance coefficient (Gijón Mancheño et al. 2021).

Adoption of Tsunami-Resilient Design Standards

Spurred by consequential events including the: Indian Ocean earthquake and tsunami (2004), Samoan earthquake and tsunami (2009), Chilean earthquake and tsunami (2010), Tohoku tsunami (2011), and Sulawesi earthquake and tsunami (2018), a number of design guidelines were proposed for vertical evacuation refuge structures (VERS) that included considerations for debris damming. An early version of this was FEMA P-646 (FEMA 2012) which accounted for "damming of accumulated waterborne debris" in Section 6.5.7. The proposed equation (Eq. 1) took a similar form to the quadratic drag law and is based on maximum momentum flux (hu^2), fluid mass density including entrained sediment (ρ_s), width of debris dam taken as the length of a standard 6.10 m (20 ft) shipping container at minimum (B_d), and an empirical drag coefficient (C_d) of 2.0. The resulting horizontal debris damming force, F_{dm}, was to be applied as a uniformly distributed load over the extents of the debris dam. Further input definitions can be found in FEMA 2012.

$$F_{dm} = \frac{1}{2}\rho_s C_d B_d (hu^2)_{max} \tag{1}$$

ASCE/SEI 7-16: Minimum Design Loads and Associated Criteria for Buildings and Other Structures included "the first national, consensus-based standard for tsunami resilience" (ASCE/SEI 2016; Chock 2016). Tsunami resilience, defined as "the ability to prepare and plan for, absorb, recover from, and more successfully adapt to adverse events" (NAS 2012), is particularly applicable to the design of VERS as well as critical and essential facilities. The current edition of these standards (ASCE/SEI 2022) includes the following tsunami loading considerations: hydrostatic, hydrodynamic, buoyancy and uplift, debris impact and damming, and foundation design parameters.

A host of experiments regarding debris impacts, particularly shipping containers and LWD, were performed in the years surrounding tsunami design adoption in 2016. Aghl et al. (2014) investigated axial impacts of shipping containers in a combined numerical and physical modelling campaign. Ko et al. (2015) investigated shipping container impacts in both air and water, employing the same error function wave generation method used in the experiment herein, as well as Bridges (2011) and Shekhar et al (2020). Ikeno et al. (2016) performed a similar physical experiment to assess the impact force of LWD at various angles of approach. While debris impact has been rigorously studied surrounding implementation of tsunami design into ASCE 7 standards, debris damming considerations have not been as thoroughly evaluated through physical model studies.

Regarding the comparison of experimental results to current tsunami-resilient design standards, pertinent sections of ASCE 7-22 (ASCE/SEI 2022) have been identified and presented here.

ASCE 7-22 identifies two alternative methods for overall lateral force-resisting system design loads. The first method, a simplified equivalent uniform lateral static pressure (ASCE 7-22 Eq. 6.10-1, Eq. 2) applies an equivalent maximum uniform pressure, p_{uw}, to account for unbalanced lateral hydrostatic and hydrodynamic loads as an initial check of the existing lateral force-resisting structure (LFRS) of the structure.

$$p_{uw} = 1.25 I_{tsu} \gamma_s h_{max} \tag{2}$$

where p_{uw} = equivalent maximum uniform pressure, applied over 1.3 times h_{max} ; I_{tsu} = tsunami importance factor; γ_s = minimum fluid weight density including entrained sediment; h_{max} = maximum inundation depth above grade plane at the structure.

The alternative method, detailed hydrodynamic lateral forces (ASCE 7-22 Eq. 6.10-2, Eq. 3), includes additional building and incident flow characteristics.

$$F_{dx} = \frac{1}{2} \rho_s I_{tsu} C_d C_{cx} B (h_{sx} u^2) \tag{3}$$

where F_{dx} = drag force on the building or structure at each level; ρ_s = minimum fluid mass density including entrained sediment ; I_{tsu} = tsunami importance factor; C_d = drag coefficient for the building as given in ASCE 7-22 Table 6.10-1; C_{cx} = proportion of closure coefficient, as calculated below; B = overall building width; h_{sx} = story height of story x; u = tsunami design flow velocity.

This method references a proportion of closure coefficient, C_{cx} (ASCE 7-22 Eq. 6.10-3, Eq. 4), taken as no less than the minimum closure ratio for load determination described in ASCE 7-22 Section 6.8.7 and 6.10.2.1 as 50% for open structures and 70% for regular structures and no more than 100%.

$$C_{cx} = \frac{\sum(A_{col} + A_{wall}) + 1.5A_{beam}}{Bh_{sx}} \tag{4}$$

where C_{cx} = proportion of closure coefficient, taken as no less than the closure ratios given in ASCE 7-22 Section 6.8.7 and 6.10.2.1; A_{col}, A_{wall} = vertical projected area of all individual column and wall elements, respectively; A_{beam} = combined vertical projected area of the slab edge and the deepest beam exposed to the flow; B = overall building width; h_{sx} = story height of story x.

This method also references an empirical drag coefficient (C_d) of the structure based on building width to inundation depth ratio, B/h, given by ASCE 7-22 Table 6.10-1. For B/h ratios less than or equal to 12, a C_d of 1.25 is used, which is representative of all tested conditions in this study. For B/h ratios equal to 60, a C_d of 1.75 is used and for B/h ratios greater than or equal to 120, a C_d of 2.0 is used. This table allows for interpolation between the C_d values.

EXPERIMENTAL SETUP

Wave Flume and Incident Wave Conditions

This experiment was performed in the Large Wave Flume (LWF) of the O.H. Hinsdale Wave Research Laboratory (HWRL) at Oregon State University (Figure 1 and 2). The LWF was 104 m long, 3.7 m wide, and 4.6 m deep with an adjustable bathymetry comprised of 3.7 m square reinforced concrete panels. The LWF was equipped with a piston-type wavemaker capable of a 4 m maximum stroke and a 4 m/s maximum stroke velocity.

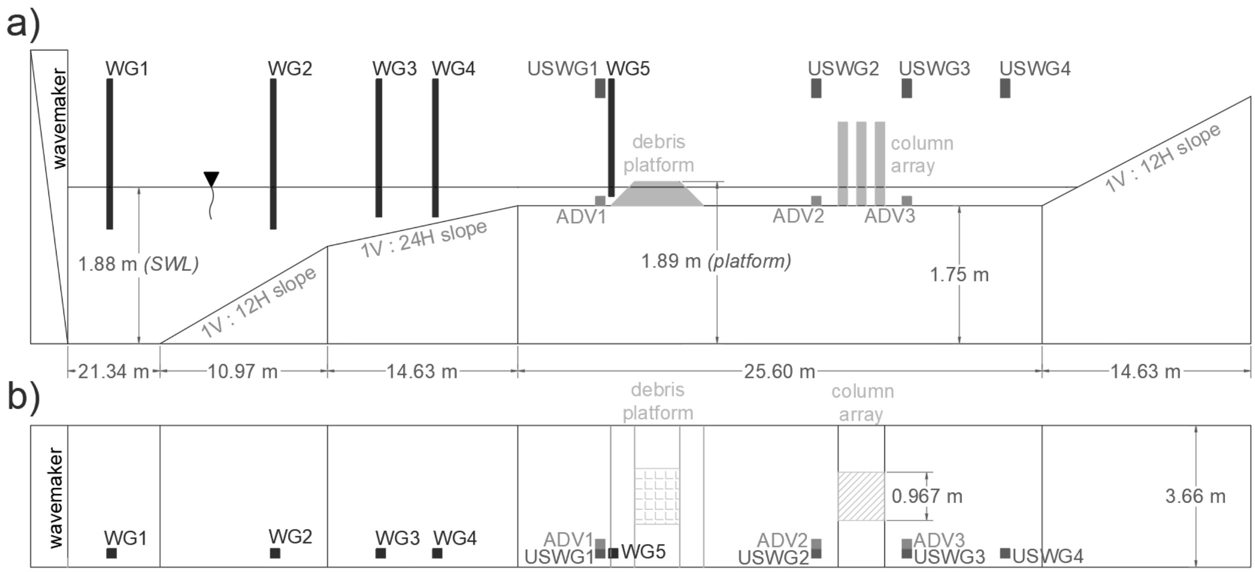

Fig 1. LWF experimental setup at HWRL (not to scale, pertinent extents shown); (a) elevation, (b) plan view; ADV = acoustic doppler velocimeter, WG = resistance wave gauge, USWG = ultrasonic wave gauge.

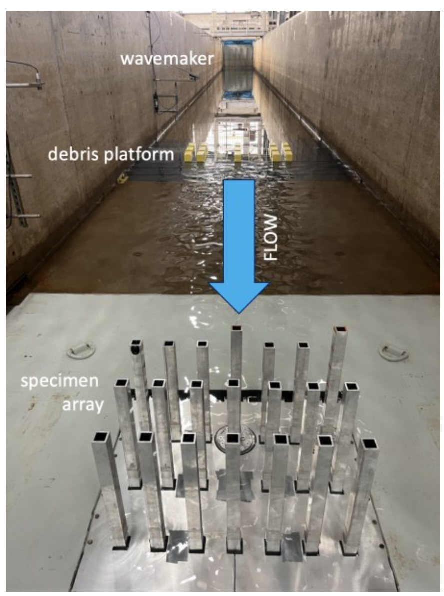

Fig 2. Annotated photo of LWF experimental setup, relative positions shown.

The bathymetric profile induced depth-limited breaking of incident waves, resulting in a broken tsunami-like bore propagating over a wet bed throughout the level test section with a local still-water line of 13 cm above the bathymetry. The bore-front turbulence and observed flow modification over the debris platform (1 cm above the 13cm still-water line) aimed to model tsunami overland flow landward of a large debris source, such as a port container facility. The coordinate space used in the LWF was as follows: + *x* in the direction of wave propagation with *x* = 0 m at the neutral position of the wavemaker; + *z* in the vertical up direction with *z* = 0 m at the LWF floor; + *y* to the left when facing the direction of wave propagation with *y* = 0 m at the centerline of the LWF.

Incident waves were generated by error function (ERF) wavemaker displacement at various scale factors (Bridges et al. 2011). Rather than conventional solitary wave generation techniques, ERF wave generation maximizes the inundation duration even for relatively small wave amplitudes by using the full 4 m wavemaker stroke. By rescaling the error function curve with the *y*-axis scaled to wavemaker displacement and the *x*-axis scaled to time of displacement (Figure 3), three incident wave conditions were selected for this experiment (Table 1, Figure 4). These three ERF scales were selected by visual observation then confirmed via Froude similitude to field studies of tsunami flow in the presence of structures (Fritz et al. 2012; Matsutomi et al. 2010), the results of which yield estimated inundation event Froude regimes between 0.4 and 2.0. While this wave generation method represents an improvement relative to solitary wave generation, the experimental inundation period and volume of water displaced is still much lower than a realistic tsunami. This has implications regarding the experimental debris dams in this study, potentially limiting debris accumulation and subsequent damming loads observed at lab scale. Incident waves are referred to as Wave A, Wave B, and Wave C herein and ERF 300, ERF 400, ERF 500 in external data structures, respectively. Hydrodynamics presented in Table 1 were recorded with a 3x7 specimen in place.

Table 1. Error function-generated incident wave maximum hydrodynamic conditions at leading (seaward) edge of column array; leading edge of column array interpolated via ADV2/ADV3 and USWG2/USWG3.

Incident wave	U_{max} *(m/s)*	η_{max} *(m)*	Fr_{max} *(-)*
Wave A	1.59	0.40	1.09
Wave B	1.27	0.35	0.92
Wave C	1.14	0.32	0.95

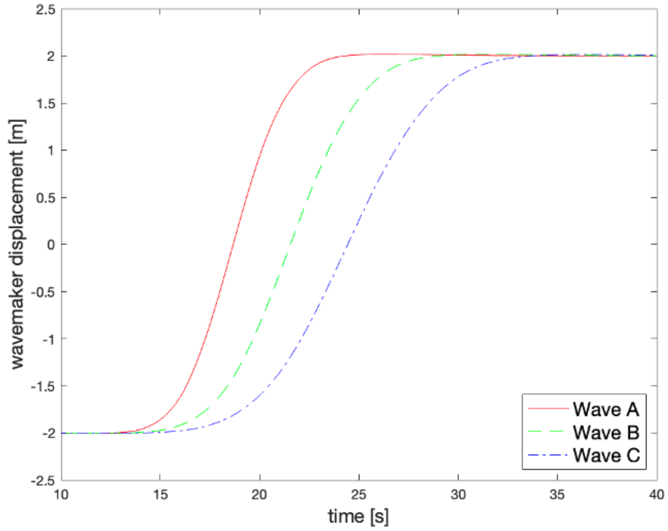

Fig 3. Wavemaker displacement during ERF wave generation.

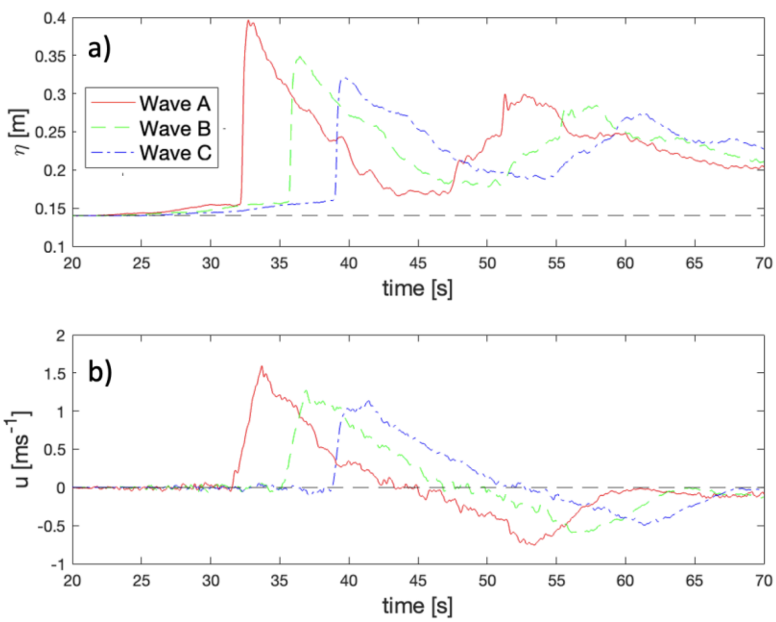

Fig 4. Mid-specimen (a) free surface displacement relative to flat test section elevation and (b) flow velocity; midpoint of column array interpolated via ADV2/ADV3 and USWG2/USWG3.

Column Specimen and Debris Elements

The experimental specimen consisted of a column array representing a pile group supporting an elevated coastal structure. The column array was underlain by a six-degree of freedom force balance plate. The column array allowed for interchangeable column configurations of 3 rows with 3, 5, or 7 columns per row (Table 2, Figure 5).

Experimental ratios of column width *(a)* to flow-perpendicular column spacing *(c)* may not be representative of prototype-scale structures, however these column dimensions were chosen to ensure the column structure remained undamaged throughout the testing campaign.

Table 2. Experimental column array configurations, showing dimensions from Figure 5.

Column configuration	Calculated C_{cx} (%)	Design C_{cx} (%)	*a* (cm)	*b* (cm)	*c* (cm)	*d* (cm)
3x3	47.5	70	5.1	96.7	40.70	22.9
3x5	79.1	79.1	5.1	96.7	17.80	22.9
3x7	110.8	100	5.1	96.7	10.17	22.9

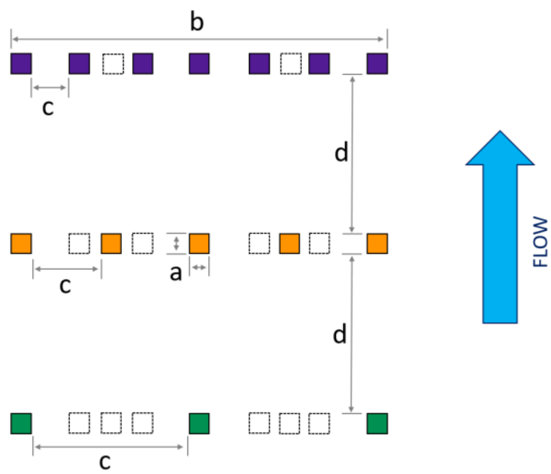

Fig 5. Schematic of column array specimen dimensions (see Table 2);
3x3 configuration = green, 3x5 configuration = orange; 3x7 configuration = purple.

Debris elements discussed in this study include 1:20 geometric scale standard 6.1 m (20 ft) and 12.2 m (40 ft) shipping containers (SC) (6.1 m SC: 0.30m L x 0.11 m W x 0.11 m H; 12.2 m SC: 0.60m L x 0.11 m W x 0.11 m H). Dimensions were informed by full-scale shipping containers but were limited by material and available manufacturing equipment. The debris elements were constructed of laminated Douglas fir lumber, then sealed and painted with orienting markings. Debris element dimensions were scaled, however masses (6.1 m SC: 2.17 kg; 12.2 m SC: 4.21 kg) were not, resulting in higher masses at prototype scale (6.1 m SC: 17,400 kg; 12.2 m SC: 33,700 kg) than fully-loaded shipping containers – provided by ASCE 7-22 Table 6.11-2: Weight and Stiffness of Shipping Container Waterborne Floating Debris – by a factor of 1.3 and 2.0 for 6.1 m and 12.2 m shipping containers, respectively. Additionally, the debris elements did not model the contents of true shipping containers shifting during impact and instead models the mass in a rigid, distributed way. Debris element masses were regularly recorded throughout testing to ensure no change in mass due to water absorption.

Instrumentation

Free-surface elevation was measured via five surface-piercing resistance wave gauges (WG, Dibble and Sollitt 1989) and four ultrasonic wave gauges (USWG, TS-30S1-IV, Senix, Hinesburg, Vermont). Flow velocity was recorded via three acoustic doppler velocimeters (ADV, Nortek Vectrino+, Nortek, Rud, Norway) which were included in hydrodynamic trials lacking debris but were removed prior to debris trials to avoid debris elements striking the submerged instruments. Sensor names, consistent with Figure 1, and locations relative to the LWF coordinate space are provided in Table 3.

Table 3. Hydrodynamic instrumentation layout relative to LWF coordinate space.

Sensor name	*X* *(m)*	*Y* *(m)*	*Z* *(m)*
WG1	10.30	-1.39	--
WG2	28.59	-1.38	--
WG3	35.89	-1.38	--
WG4	39.55	-1.37	--
WG5	50.48	-1.46	--
USWG1	50.51	-0.93	3.03
USWG2	57.79	-1.37	3.33
USWG3	61.44	-1.36	3.33
USWG4	68.76	-1.37	3.33
ADV1	50.49	-1.29	1.77
ADV2	57.79	-1.64	1.77
ADV3	61.42	-1.65	1.77

The full column array was underlain by a six-degree of freedom force balance plate (FBP, AF 32-12-K, AMTI, Watertown, MA) to measure total forces and moments acting on the array. An additional six-degree of freedom pancake load cell (LC, Omega191 SI 7200-1400, ATI, Apex, North Carolina) was installed atop the FBP to record forces and moments acting on the center column of the seaward row individually.

Plan view recordings of the full experimental extents- debris platform through column specimen- were captured via four down-facing 4K HD CCTV cameras (RLC-810A, Reolink, New Castle, Delaware) with overlapping fields of view. An isometric view of the column array was captured via another camera (HERO11 Black, GoPro, San Mateo, California) mounted on the LWF wall above the still water level.

METHODS

Experimental Procedure

Prior to column array installation, preliminary trials were performed to identify the debris orientation that maximized the number of debris elements passing through the column array footprint. During later debris trials, the quantity and orientation of debris was kept consistent for each debris type, shown in Figure 6.

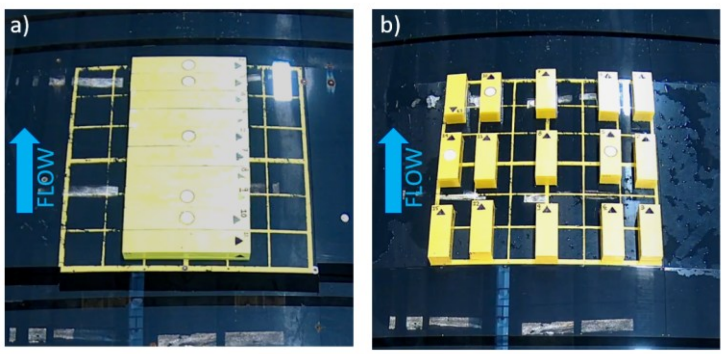

Fig 6. Initial debris element configuration on debris platform and inundation flow direction for (a) 12.2 m shipping container and (b) 6.1 m shipping container debris elements.

For each experimental trial (Figure 7), the data acquisition system (DAQ) was started, triggering the force balance plate (FBP) and hydrodynamic instruments, while cameras were started manually. Video recordings were later synchronized with the corresponding data by referencing bore arrival at the seaward row of columns. DAQ and FBP time-series were recorded for 200 seconds, the DAQ sampling at 100Hz and the FBP sampling at 1000Hz. Video recordings were stopped manually upon completion of return flow, upon which the research team would enter the flume to reset debris for the succeeding trial. Following the resetting of debris, the flume was left undisturbed as free-surface variations settled out, resulting in approximately 20 minutes elapsed between successive trials.

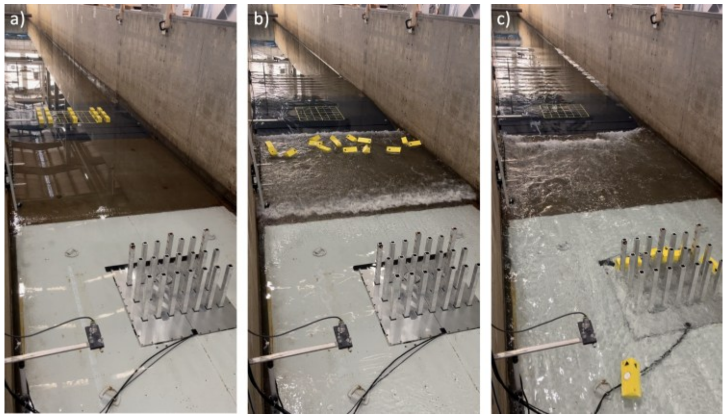

Fig 7. Example experimental trial (Wave C, 6.1 m SC, 3x7 column array) showing phases of a) pre-bore arrival, b) debris transport, and c) debris damming against structure.

Photogrammetry Analysis

A method for photogrammetric analysis of in-situ debris dams was developed and validated to estimate submerged projected areas of experimental debris dams. Debris dams were then analyzed using this method at times of horizontal force local maxima during both debris accumulation and quasi-steady phases of debris damming (Figure 8). Samples from both phases were included in the analyzed data. Debris dams were classified as either debris accumulation phase while debris were still actively aggregating against the column array or as quasi-steady phase when the debris dam was no longer subject to further debris accumulation or reshuffling under the inundation flow. It should be noted that experimental debris dams were analyzed via this photogrammetric method during the inundation flow phase, not following the conclusion of each trial when debris settled against flume bathymetry. Raw FBP horizontal force data was low-pass filtered to isolate the debris damming signal (after Shekhar et al. 2020) with frequencies above 5 Hz filtered out , frequencies below 2.5 Hz retained, and a weighted transition zone between 2.5 and 5 Hz, as shown in Figure 8.

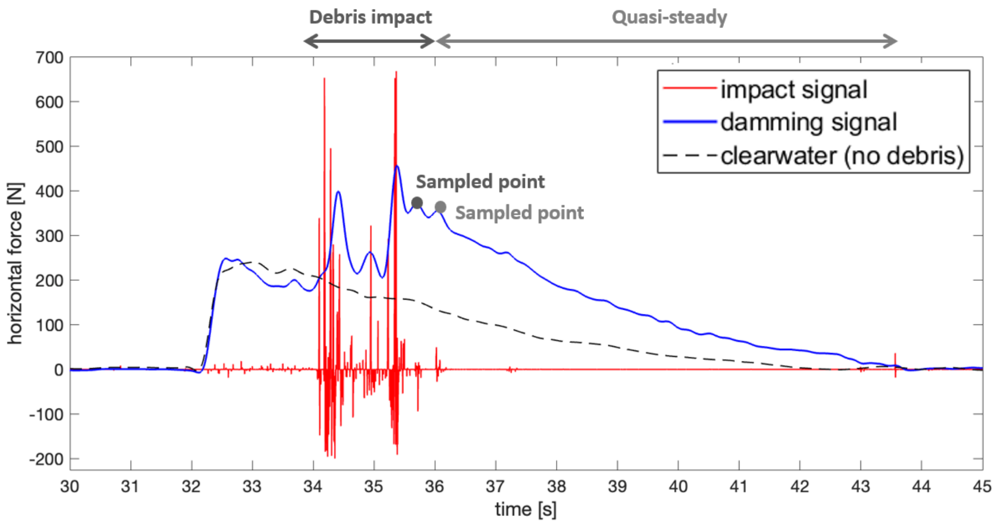

Fig 8. Example FBP time-series showing filtered out debris impact signal (red), retained debris damming signal isolated via weighted low-pass filtering (blue), and low-pass filtered clearwater force (black dashed line), for comparison.

At each timestamp of photogrammetric analysis, the following method was performed: First, damming angle of each element relative to the incident flow was estimated at 15 degree intervals and a raw projected area was calculated via trigonometric projection of a rectangular prism. Next, the proportion of each element exposed to incident flow was estimated as a percent area by visual inspection of synchronized video perspectives, correcting for shielding and overlapping of debris and resulting in a corrected projected area. Next, the submerged proportion of each element was similarly estimated, again by visual estimation of percent area, correcting for incomplete submersion and resulting in a submerged projected area. Finally, the submerged projected area of any columns not shielded by debris was calculated and summed along with the element-wise submerged projected areas of all debris elements.

This photogrammetric method was validated using 26 dam test cases, in which debris type, quantity, position, damming angle, and water depth were varied to replicate debris dams similar to those observed in the experiment. For each dam test case, the following method was performed (Figure 9): Video was recorded circumscribing the column array, including the test case debris elements and a 1 m reference square (Fig 9a), then converted to a three-dimensional point cloud (Fig 9b). Next, the three-dimensional point cloud was rectified into a flow-aligned orthographic projection (Fig 9c). The flow-aligned orthographic projection was imported into a CAD program (AutoCAD 2022, Autodesk) and re-scaled based upon the 1 m reference square (Fig 9d). Finally, projected area of the test case was outlined and measured, with an approximate 5% error based on known dimensions of the column specimen.

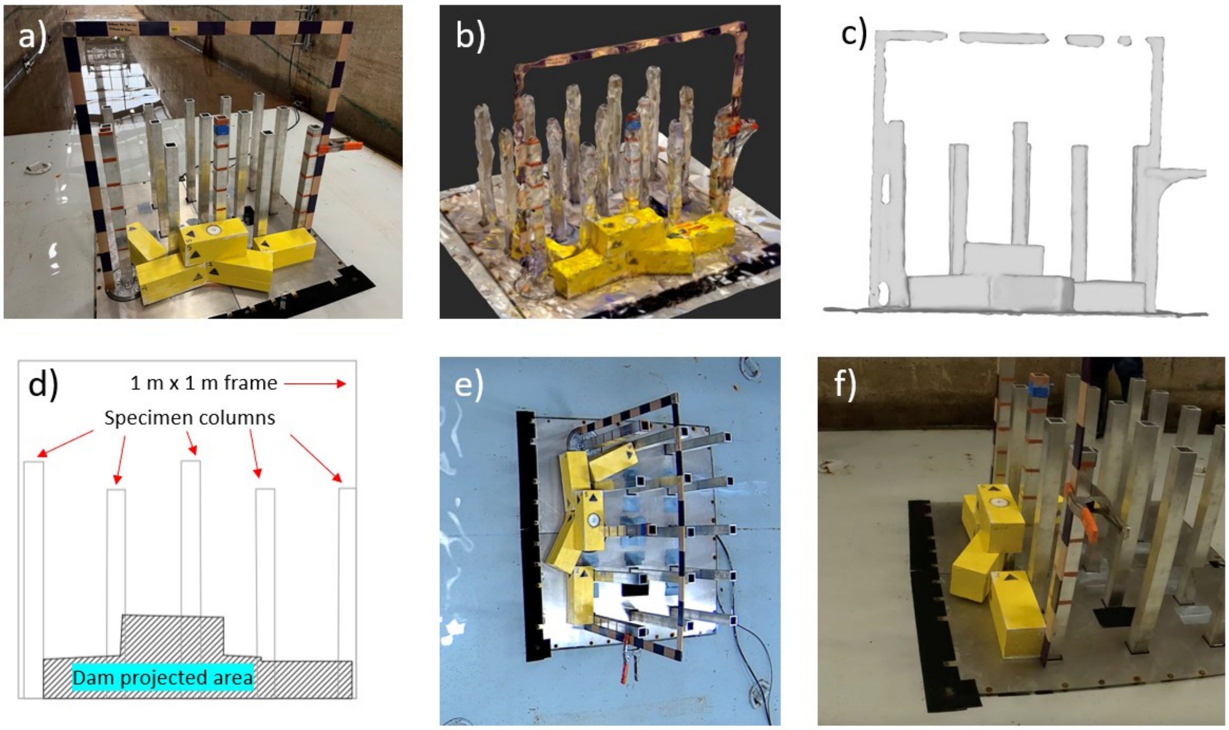

Fig 9. Debris dam test case projected area calculation for photogrammetry method validation; (a) example test case; (b) three-dimensional .obj file of scanned test case; (c) flow-aligned orthographic projection of scanned test case; (d) measured projected area of test case, re-scaled in AutoCAD according to 1 m reference frame; (e) plan view and (f) isometric view of test case used during photogrammetry method analysis.

These measured areas of dam test cases were then compared to estimated areas obtained via the proposed photogrammetric method. The 26 test cases were subdivided as a means of validating specific attributes of the photogrammetric method: 10 cases estimating total projected area in 4 cm of water (total projected area, minimal confounding effects of submersion), 8 cases estimating total projected area in 13 cm of water (total projected area, increased effects of submersion), and 8 cases estimating submerged projected area in 13cm of water (full intended scope of photogrammetric method). Validation results are shown in Table 4 and Figure 10, resulting in 5% mean absolute percentage error in estimated submerged projected areas of experimental debris dams.

Table 4. Summary of photogrammetric method validation results

Estimated value	SWL (cm)	Root-mean-square error (m^2)	Mean absolute percentage error (%)
total projected area, A_p	4.0	0.0081	6.9
total projected area, A_p	13.0	0.0020	2.9
submerged projected area, A_{sp}	13.0	0.0034	5.0

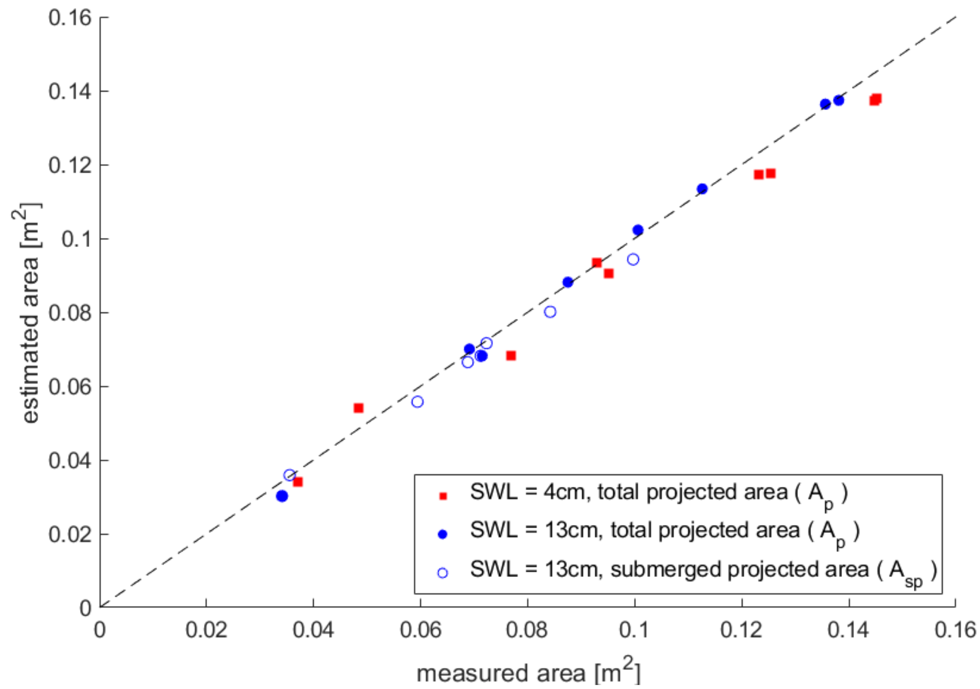

Fig 10. Results of photogrammetric method validation campaign.

ANALYSIS

Table 5 summarizes experimental debris damming horizontal forces at local maxima during both debris accumulation and quasi-steady phases (as shown in Figure 8) in comparison to lateral force-resisting system (LFRS) design loads per ASCE 7-22 Section 6.10 (ASCE/SEI 2022). Mean factor of safety (FS_{mean}) is calculated as the LFRS design load divided by the mean experimental debris damming horizontal force for each set of conditions.

Table 5. Summary of experimental debris damming horizontal forces to ASCE 7-22 Section 6.10 lateral force-resisting system design loads given by ASCE 7-22 Equations 6.10-1 and 6.10-2 (Eq. 2 and 3, respectively).

Wave	Specimen	Mean (N)	SD (N)	Eq. 6.10-1 (N)	FS mean	Eq. 6.10-2 (N)	FS mean
A	3x3	268.1	113.2	3391	12.6	588.2	2.19
	3x5	298.5	104.0	3391	11.4	664.7	2.23
	3x7	333.2	117.3	3391	10.2	840.4	2.52
B	3x3	164.0	57.9	2596	15.8	328.4	2.00
	3x5	201.9	52.7	2596	12.9	371.1	1.84
	3x7	214.9	88.5	2596	12.1	469.1	2.18
C	3x3	97.4	39.0	2170	22.3	286.2	2.94
	3x5	126.5	41.0	2170	17.2	323.4	2.56
	3x7	128.6	22.0	2170	16.9	408.9	3.18

ASCE 7-22 Equation 6.10-1 (Eq. 2) represents the simplified equivalent uniform lateral static pressure intended in the commentary as a "conservative alternative to more detailed tsunami loading analysis. This equation is based on the assumption that all of the most conservative provisions presented elsewhere in this section occur simultaneously on a rectangular building with no openings" (ASCE/SEI 2022). This value was calculated for each wave condition, applied as a uniform pressure over the vertical plane area defined as the cross-flume width of the column array (B = 0.967 m) and the height of 1.3 times the maximum inundation depth (h_{max}). Because the column array was intended to model a vertical evacuation refuge structure (VERS) or critical facility, a tsunami importance factor (I_{tsu}) of 1.25 is applied throughout this analysis.

Table 5 shows that ASCE 7-22 Equation 6.10-1 (Eq. 2) performs as expected under the tested experimental conditions, with mean factors of safety averaging 14.6, thus representing a high degree of design conservatism. For all three incident wave conditions, the mean factor of safety decreases as column density increases. This is anticipated, as this simplified method treats the structure as a solid vertical plane area rather than factoring column density into design load calculations, yielding a single design load for all three column configurations subject to a given wave condition. Conservatism increases as incident wave energy decreases, with mean factors of safety averaging 11.4, 13.6, and 18.8 for Waves A, B, and C, respectively. As an initial check of a structure's existing LFRS to determine whether more detailed loading analysis is required, such high mean factors of safety reflect a high degree of design conservatism, indicating that ASCE 7-22 Equation 6.10-1 (Eq. 2) performs as intended under the tested conditions of this experiment.

Figure 11 shows experimental debris damming horizontal forces compared to ASCE 7-22 Eq. 6.10-2 (Eq. 3) for detailed lateral-force-resisting system design loads. This approach is used in design if the existing LFRS capacity fails to exceed the design load given by the previous simplified method, ASCE 7-22 Equation 6.10-1 (Eq. 2). Applied to this experimental model, C_{cx} was taken as 0.70, 0.79, and 1.00 for the 3x3, 3x5, and 3x7 column configurations, respectively (Table 2). I_{tsu} was again taken as 1.25 and h_{sx} was taken as h_{max} for each incident wave condition, a measure to better apply Eq. 3 to this idealized model of a column array. Here, horizontal forces are plotted against instantaneous inundation Froude number at the specimen seaward face, calculated as:

$$Fr = \frac{u}{\sqrt{g(\eta)}} = \frac{u}{\sqrt{g(H+h)}} \tag{5}$$

where Fr = instantaneous inundation Froude number; u = instantaneous inundation flow velocity; g = gravitational acceleration; η = instantaneous free surface elevation above flume bathymetry; H = instantaneous bore height above still water level (SWL); h = still water level (SWL), a constant 13 cm for all experimental trials.

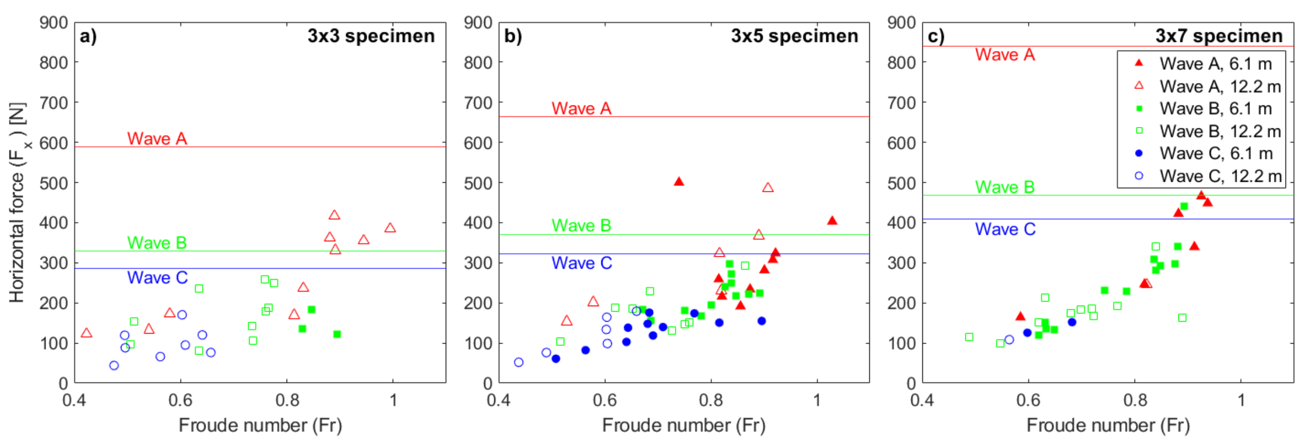

Fig 11. Comparison of experimental debris damming horizontal forces to ASCE 7-22 Eq. 6.10-2 (Eq. 3) for lateral-force-resisting system design loads.

Figure 11 demonstrates that ASCE 7-22 Equation 6.10-2 (Eq. 3) performs as expected under the tested experimental conditions, with no experimental debris damming horizontal force exceeding the corresponding design load for the conditions of that trial. As anticipated, debris damming forces generated by Wave A (red triangles) generally exceed those generated by Wave B (green squares), which generally exceed those generated by Wave C (blue circles). This trend reflects the similar form that ASCE 7-22 Equation 6.10-2 (Eq. 3) takes to the quadratic drag law, with a dependence on a velocity-squared term. Correspondingly, higher instantaneous Froude regimes generally lead to higher experimental horizontal debris damming forces.

Table 5 also provides mean factors of safety for ASCE 7-22 Equation 6.10-2 (Eq. 3), all far less than the corresponding mean factors of safety for ASCE 7-22 Equation 6.10-1 (Eq. 2). This affirms that the former is a more detailed design approach, should the latter fail to be satisfied by the existing LFRS of a structure. For Waves A, B, and C, mean factors of safety are similar across all column configurations of 2.3, 2.0, and 2.9, respectively. Regarding column configuration, mean factors of safety show averages across all incident wave conditions of 2.3, 2.2, and 2.6 for 3x3, 3x5, and 3x7 column configurations, respectively. Across all tested experimental conditions, ASCE 7-22 Equation 6.10-2 (Eq. 3) yields a mean factor of safety of 2.4. This, along with no experimental debris damming horizontal force exceeding the corresponding design load, indicates that ASCE 7-22 Equation 6.10-2 (Eq. 3) is conservative across all tested experimental conditions.

Figure 12 shows experimental proportion of closure coefficients (C_{cx}) in comparison to design C_{cx} values given by ASCE 7-22 Section 6.8.7 and 6.10.2.1. Estimated submerged projected dam areas, calculated via the proposed photogrammetry method, are added to the projected areas of any unsheltered seaward columns and that of all middle and landward columns to obtain a total estimated submerged projected area (A_{sp}) for the structure under debris damming. This estimated value is then divided by the vertical plane area defined as the cross-flume width of the column array (B = 0.967 m) times the maximum inundation depth (h_{max}) of the given incident wave to obtain the experimental C_{cx} shown. ASCE 7-22 Section 6.8.7 prescribes a minimum design closure ratio of 0.7 for the 3x3 column configuration. ASCE 7-22 Section 6.10.2.1 prescribes a design C_{cx} of 0.79 for the 3x5 column configuration and a maximum C_{cx} of 1.0 for the 3x7 column configuration, due to column scaling effects.

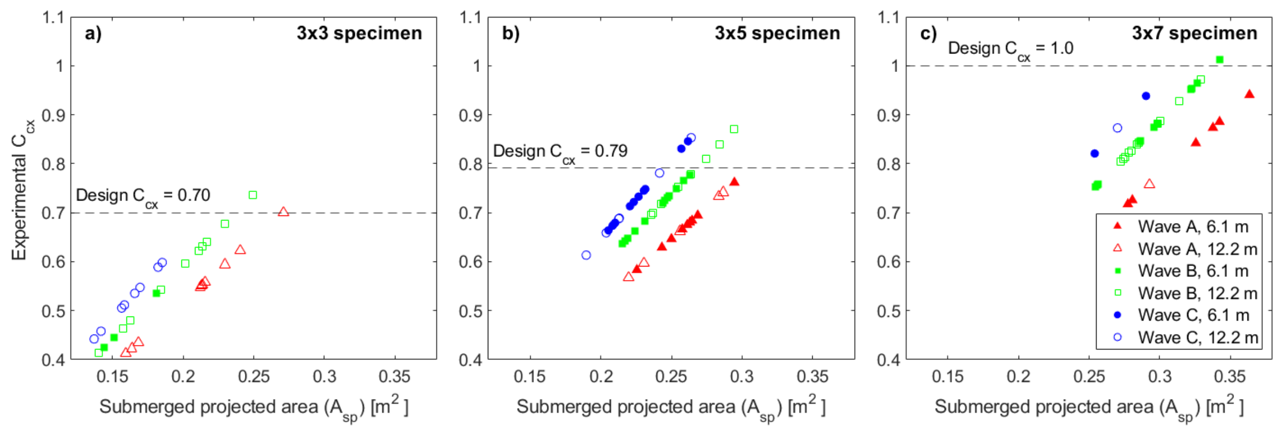

Fig 12. Comparison of experimental to design proportion of closure coefficients (C_{cx}).

Figure 12 shows that design proportion of closure coefficients (C_{cx}) per ASCE 7-22 Section 6.8.7 generally perform as expected under the tested conditions of this experiment. For the 3x3 column configuration, the minimum design C_{cx} of 0.7 was exceeded by 2 individual trials, both with larger (12.2 m shipping container) debris elements. For the 3x5 column configuration, the prescribed design C_{cx} of 0.79 was exceeded by multiple trials under both Wave B and C, however this did not affect the design conservatism of ASCE 7-22 Equation 6.10-2 (Eq. 3), as shown in Figure 11. For the 3x7 column configuration, the prescribed design C_{cx} of 1.0 was exceeded only once, due to debris elements overhanging the cross-flume extents of the specimen footprint.

Figure 13 shows bulk resistance coefficients of the tested column array configurations aggregated from all three incident wave conditions. These data were obtained by sampling hydrodynamic (no debris) data (recorded and sampled at 100 Hz) and horizontal force data (recorded at 1000 Hz, downsampled at 100 Hz to match hydrodynamic data) over the inundation flow duration (when inundation flow velocity, u, exceeds 10% of u_{max}) and calculating resistance coefficient via a modified quadratic drag equation (Mauti et al. 2020, Eq. 3). The vertical dashed line represents the drag coefficient of 1.25 proposed by ASCE 7-22 Table 6.10-1 based upon the width to inundation depth ratios of this experimental model.

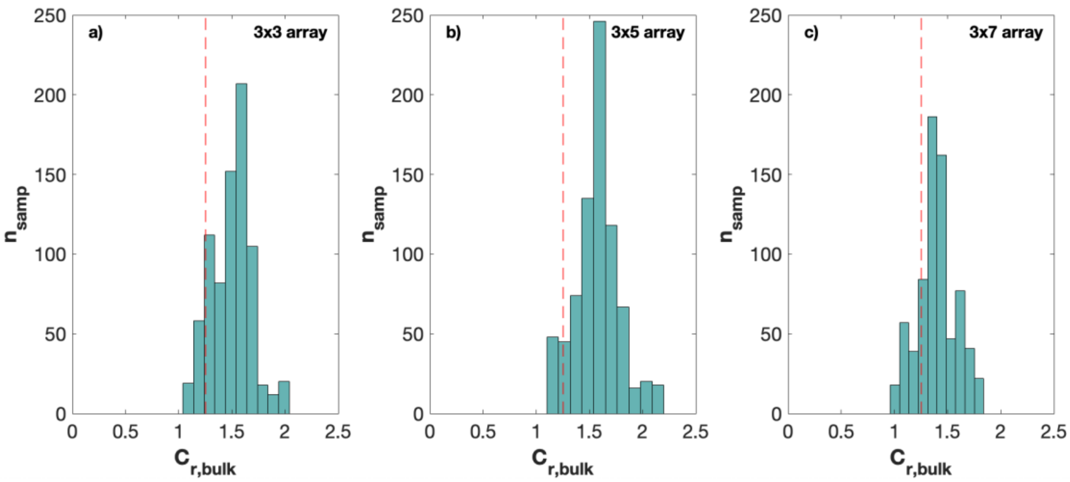

Fig 13. Comparison of experimental bulk resistance coefficients *($C_{r,\ bulk}$)* to ASCE 7-22 Table 6.10-1 drag coefficients for rectilinear structures; ASCE 7-22 Table 6.10-1 drag coefficient *(C_d)* shown by vertical red dashed line.

Table 5. Hydrodynamic bulk resistance coefficient summary statistics of each column configuration.

Specimen	ASCE 7-22 (C_d)	Mean ($C_{r,\ bulk}$)	SD ($C_{r,\ bulk}$)	Median ($C_{r,\ bulk}$)
3x3	1.25	1.50	0.19	1.52
3x5	1.25	1.58	0.21	1.58
3x7	1.25	1.40	0.18	1.40

Figure 13 and Table 5 show that for all tested column configurations, experimental hydrodynamic bulk resistance coefficients *($C_{r,\ bulk}$)* regularly exceed the design drag coefficient (C_d) given by ASCE 7-22 Table 6.10-1 for the building depth to inundation depth ratios of this experiment. There is variability between mean $C_{r,\ bulk}$ values of the tested column configurations, likely due to variation in intercolumn effects of blockage and sheltering. Blockage is known to increase local flow velocity by channeling flow between flow-perpendicular obstructions while sheltering is known to decrease local flow velocity due to upstream obstructions shielding flow (Gijón Mancheño et al. 2021).

DISCUSSION

Both design load calculations for tsunami vertical evacuation refuge structures (VERS) provided in ASCE 7-22 Section 6.10 were shown to be conservative across all tested experimental conditions. ASCE 7-22 Equation 6.10-1 is intended as a preliminary check of a structure's lateral force-resisting system (LFRS) to resist tsunami-induced unbalanced lateral hydrostatic and hydrodynamic loads. As expected for the scope of this equation, the mean factor of safety (FS) for this method was 14.6 relative to experimental debris damming horizontal forces, indicating sufficient design conservatism.

Should the LFRS of a structure fail to satisfy this above initial check, a more detailed design load calculation is to be performed per ASCE 7-22 Equation 6.10-2 (Eq. 3). This method involves additional terms for site-specific building and flow characteristics, including considerations for variable column density, an overall building drag coefficient, and a dependence on flow velocity-squared, akin to the quadratic drag law. As presented in Table 5 and Figure 11, this design load calculation was shown to be conservative across all tested conditions. The experimental results yielded an overall mean factor of safety of 2.4, indicating closer agreement between experimental forces and design loads while still maintaining design conservatism for this more detailed method. Additionally, no instances of an experimental debris damming horizontal force exceeding the corresponding design load were observed. This indicates that even under the most extreme conditions simulated by this experiment, yielding the largest experimental debris damming forces, ASCE 7-22 Equation 6.10-2 (Eq. 3) maintained design conservancy. Intended as a more comprehensive approach following an initial capacity check from ASCE 7-22 Equation 6.10-1 (Eq. 2), this detailed method exhibited a lower factor of safety in general, but maintained design conservatism and therefore performed as expected based on the intended application.

Figure 12 shows that proportion of closure coefficients (C_{cx}) used in design were generally conservative across the tested experimental conditions. While the design C_{cx} value was exceeded at least once for each column configuration, Figure 11 and Table 5 indicate that this exceedance did not affect design load conservatism of ASCE 7-22 Equation 6.10-2 (Eq. 3). Instances of exceedance were more often than not due to larger debris elements (12.2 m shipping containers) and/or debris overhanging the cross-flume extents of the column array. Caution should be taken in this assessment of conservatism, however, since laboratory modeling of tsunami debris damming may not yield the same closure as observed in full-scale design level tsunami events (Carden et al., 2015). The scope of this analysis of experimental C_{cx} values, derived by employing a new photogrammetric method, intends to assess experimental closure due to modeled debris accumulation against the specimen. The proposed photogrammetry method allowed for this level of detailed in-situ analysis and may be used in later phases of this experimental campaign. Additional work including varied building and column dimensions, varied debris element dimensions, and denser, heterogeneous debris fields may help to investigate such structural closure phenomena.

Figure 13 shows that the drag coefficients for rectilinear structures given by ASCE 7-22 Table 6.10-1 do not capture those experimentally determined under the tested column configurations. Since the original publication of this table in ASCE 7-16 (ASCE/SEI 2016), multiple tsunami-related publications have adopted the use of resistance coefficient rather than drag coefficient (Stolle et al. 2018, Mauti et al. 2020). This is particularly applicable to surface-piercing obstacles, like partially inundated structures, and accounts for flow-column interactions that may not be captured in drag coefficients for rectilinear structures of the same exterior dimensions.

Mean $C_{r,\,bulk}$ for the 3x7 column configuration is closest to the value given by ASCE 7-22 Table 6.10-1, likely due to increased sheltering effect reducing inundation flow velocity on the second and third rows of the column array. Mean $C_{r,\,bulk}$ for the 3x3 column configuration is slightly further from the value given by ASCE 7-22 Table 6.10-1. Such a sparse seaward row of columns likely limits the effects of sheltering, but in turn also limits blockage effects. In other words, seaward columns may have little sheltering effect on subsequent rows, but also may not drastically channelize flow and increase flow velocity on downstream columns. Mean $C_{r,\,bulk}$ for the 3x5 column configuration is greatest compared to the value given by ASCE 7-22 Table 6.10-1. Relative to the 3x3 column configuration, blockage effects and sheltering effects are both likely to increase. Due to the relatively large stream-wise spacing of the column array, the increase in blockage likely outweighs the increase in sheltering, leading to a higher mean value of $C_{r,\,bulk}$.

A major benefit of discussing flow resistance in terms of bulk resistance coefficient is that these sheltering, blockage, and unbalanced hydrostatic force effects are all captured in addition to the form drag contribution of the structure (Stolle et al. 2018). The growth of "resistance coefficient" in tsunami literature represents a potential improvement in nomenclature while a "bulk" dimensionless parameter captures intercolumn effects that the rectilinear structure definition given by ASCE 7-22 Table 6.10-1 may not fully reflect.

It should be noted that several assumptions were made in this physical model. At 1:20 geometric scaling, the 5.1 cm wide columns would be 1.02 m wide at prototype scale, likely too wide to accurately represent columns of

VERS. Column scaling is likely to be improved in later phases of this experimental campaign. Further, flows at such shallow depths are more sensitive to bottom friction, thus affecting roughness and viscosity in terms of Reynolds scaling. Such scaling effects may lead to differences in these results compared to other similar studies or full-scale applications of ASCE 7-22 standards. Additionally, due to laboratory limitations on water displacement and inundation duration, the experimentally generated debris dams may not have developed representatively of real-world debris dams subject to longer inundation durations. Similarly, the volume and quantity of incident debris was limited, potentially misrepresenting the volume and density of real-world debris fields (Nistor et al. 2017). Finally, due to the transient nature of tsunami inundation flow, projected areas of debris dams were quantified as best as possible via the photogrammetric method explained herein, yet these are still to be taken as estimates.

CONCLUSIONS

The findings presented here represent comparisons of experimental debris damming metrics to those considered in ASCE 7-22 Chapter 6: Tsunami Loads and Effects (ASCE/SEI 2022). Based on the results of this physical model experiment of tsunami debris damming forces:

1. ASCE 7-22 Equation 6.10-1 (Eq. 2), simplified equivalent uniform lateral static pressure, is conservative across all tested experimental conditions and performs as expected given the intended scope;
2. ASCE 7-22 Equation 6.10-2 (Eq. 3), detailed hydrodynamic lateral forces, yields lower mean factors of safety but maintains design conservatism across all tested experimental conditions, also performing as expected given the intended scope;
3. ASCE 7-22 Section 6.8.7 and 6.10.2.1 design proportion of closure coefficients are conservative across the majority of tested experimental conditions, and instances of unconservatism do not induce unconservative load estimation in ASCE 7-22 Equation 6.10-2 (Eq. 3);
4. ASCE 7-22 Table 6.10-1 drag coefficients for rectilinear structures are often exceeded by experimental hydrodynamic bulk resistance coefficients; and
5. Bulk resistance coefficient may represent an improved dimensionless measure of flow resistance than drag coefficients currently used in ASCE 7-22 load predictions.

This study represents a preliminary comparison of lab-scale experimental data to ASCE 7-22 tsunami-resilient design standards. Additional trials and similar studies should yield an improved understanding of debris damming forces on elevated structures. More work is needed to continue this investigation, particularly with varying structure and debris characteristics, to further assess the findings presented here.

DATA AVAILABILITY STATEMENT

Data from this experiment are available on DesignSafe.org. (Provide full citations that include URLS or DOIs.)

ACKNOWLEDGEMENTS

Funding for this research was provided by the National Science Foundation (NSF) Division of Civil, Mechanical, and Manufacturing Innovation (CMMI) and Natural Hazards Engineering Research Infrastructure (NHERI) through Grants #2203131, #2203116 and #2037914. The authors would like to thank the HWRL and CEOAS Machine and Technical Development Facility staff for their assistance in experimental setup and testing.

REFERENCES:

Aghl PI, CJ Naito, HR Riggs (2015) "Estimation of demands resulting from inelastic axial impact of steel debris." Engineering Structures, 82, 11–21. https://doi.org/10.1016/j.engstruct.2014.10.021

Arnason H, C Petroff, H Yeh (2009) "Tsunami bore impingement onto a vertical column." Journal of Disaster Research, 4(6), 391–403. https://doi.org/10.20965/jdr.2009.p0391

ASCE/SEI (2016) "Minimum design loads for buildings and other structures." ASCE/SEI 7-16, Reston, VA.

ASCE/SEI (2022) "Minimum design loads for buildings and other structures." ASCE/SEI 7-22, Reston, VA.

Bridges K, D Cox, S Thomas, S Shin, M Rueben (2011) "Large-scale wave basin experiments on the influence of large obstacles on tsunami inundation forces." Coastal Structures. https://doi.org/10.1142/9789814412216_0107

Bocchiola D, MC Rulli, R Rosso (2006) "Transport of large woody debris in the presence of obstacles." Geomorphology, 76(1–2), 166–178. https://doi.org/10.1016/j.geomorph.2005.08.016

Carden L, G Chock, G Yu, I Robertson (2015) "The new ASCE tsunami design standard applied to mitigate Tohoku tsunami building structural failure mechanisms." Handbook of Coastal Disaster Mitigation for Engineers and Planners, 461–490. https://doi.org/10.1016/b978-0-12-801060-0.00022-8

Chaplin JR, P Teigen (2003) "Steady flow past a vertical surface-piercing circular cylinder." Journal of Fluids and Structures, 18(3–4), 271–285. https://doi.org/10.1016/j.jfluidstructs.2003.07.009

Chock GY (2016) "Design for tsunami loads and effects in the ASCE 7-16 standard." Journal of Structural Engineering, 142(11). https://doi.org/10.1061/(asce)st.1943-541x.0001565

Dibble TL, CK Sollitt (1989) "New designs for acoustic and resistive wave profiles." In Proc., Workshop on Instrumentation for Hydraulic Laboratories, 185–200. Ottawa: International Association for Hydro-Environment Engineering and Research.

Federal Emergency Management Agency (2012) "6. Load Determination and Structural Design Criteria." In Guidelines for Design of Structures for Vertical Evacuation from Tsunamis (Second, pp. 90–91).

Federal Emergency Management Agency (2019) "A. Vertical Evacuation Structure Examples." In Guidelines for Design of Structures for Vertical Evacuation from Tsunamis (Third, pp. A-1).

Fenton JD (2003) "The effects of obstacles on surface levels and boundary resistance in open channels." Proc. 30th IAHR Congress, Thessaloniki, 24-29 August 2003, eds J. Ganoulis and P. Prinos, Vol. C2, pp9-16.

Fritz HM, DA Phillips, A Okayasu, T Shimozono, H Liu, F Mohammed, V Skanavis, CE Synolakis, T Takahashi (2012) "The 2011 Japan tsunami current velocity measurements from survivor videos at Kesennuma Bay Using Lidar." Geophysical Research Letters, 39(7). https://doi.org/10.1029/2011gl050686

Gijón Mancheño A, W Jansen, JC Winterwerp. Predictive model of bulk drag coefficient for a nature-based structure exposed to currents. Sci Rep 11, 3517 (2021). https://doi.org/10.1038/s41598-021-83035-0

Ikeno M, D Takabatake, N Kihara, H Kaida, Y Miyagawa, A Shibayama (2016) "Improvement of collision force formula for woody debris by airborne and hydraulic experiments." Coastal Engineering Journal, 58(4). https://doi.org/10.1142/s0578563416400222

Ko HT-S, DT Cox, HR Riggs, CJ Naito (2015) "Hydraulic experiments on impact forces from tsunami-driven debris." Journal of Waterway, Port, Coastal, and Ocean Engineering, 141(3). https://doi.org/10.1061/(asce)ww.1943-5460.0000286

Matsutomi H, K Okamoto (2010) "Inundation flow velocity of tsunami on land." Island Arc, 19(3), 443–457. https://doi.org/10.1111/j.1440-1738.2010.00725.x

Mauti G, J Stolle, T Takabatake, I Nistor, N Goseberg, A Mohammadian (2020) "Experimental investigation of loading due to debris dams on structures." Journal of Hydraulic Engineering, 146(5). https://doi.org/10.1061/(asce)hy.1943-7900.0001731

Naito C, C Cercone, HR Riggs, D Cox (2014) "Procedure for site assessment of the potential for Tsunami Debris Impact." Journal of Waterway, Port, Coastal, and Ocean Engineering, 140(2), 223–232. https://doi.org/10.1061/(asce)ww.1943-5460.0000222

National Academy of Sciences (2012) "Disaster resilience—A national imperative." National Academies Press, Washington, DC.

Nistor I, N Goseberg, J Stolle (2017) "Tsunami-driven debris motion and loads: A critical review." Frontiers in Built Environment, 3. https://doi.org/10.3389/fbuil.2017.00002

Oudenbroek K, N Naderi, J Bricker, Y Yang, C van der Veen, W Uijttewaal, S Moriguchi, S Jonkman (2018) "Hydrodynamic and debris-damming failure of bridge decks and piers in steady flow." Geosciences, 8(11), 409. https://doi.org/10.3390/geosciences8110409

Park H, MJ Koh, DT Cox, MS Alam, S Shin (2021) “Experimental study of debris transport driven by a tsunami-like wave: Application for non-uniform density groups and obstacles.” Coastal Engineering, 166, 103867. https://doi.org/10.1016/j.coastaleng.2021.103867

Qi ZX, I Eames, ER Johnson (2014) "Force acting on a square cylinder fixed in a free-surface channel flow." Journal of Fluid Mechanics, 756, 716–727. https://doi.org/10.1017/jfm.2014.455

Robertson IN, HR Riggs, SC Yim, YL Young (2007) "Lessons from Hurricane Katrina storm surge on bridges and buildings." Journal of Waterway, Port, Coastal, and Ocean Engineering, 133(6), 463–483. https://doi.org/10.1061/(asce)0733-950x(2007)133:6(463)

Saatcioglu M, A Ghobarah, I Nistor (2005) "Effects of the December 26, 2004 Sumatra Earthquake and Tsunami on Physical Infrastructure." ISET Journal of Earthquake Technology, 42(4), 79–94.

Schmocker L, WH Hager (2011) "Probability of drift blockage at bridge decks." Journal of Hydraulic Engineering, 137(4), 470–479. https://doi.org/10.1061/(asce)hy.1943-7900.0000319

Shekhar K, AO Winter, MS Alam, P Arduino, GR Miller, MR Motley, MO Eberhard, AR Barbosa, P Lomonaco, DT Cox (2020) "Conceptual evaluation of tsunami debris field damming and impact forces." Journal of Waterway, Port, Coastal, and Ocean Engineering, 146(6). https://doi.org/10.1061/(asce)ww.1943-5460.0000600

Stolle J, T Takabatake, I Nistor, T Mikami, S Nishizaki, G Hamano, H Ishii, T Shibayama, N Goseberg, E Petriu (2018) "Experimental investigation of debris damming loads under transient supercritical flow conditions." Coastal Engineering, 139, 16–31. https://doi.org/10.1016/j.coastaleng.2018.04.026

Stolle J, C Krautwald, I Robertson, H Achiari, T Mikami, R Nakamura, T Takabatake, Y Nishida, T Shibayama, M Esteban, I Nistor, N Goseberg (2020) "Engineering lessons from the 28 September 2018 Indonesian tsunami: Debris Loading." Canadian Journal of Civil Engineering, 47(1), 1–12. https://doi.org/10.1139/cjce-2019-0049

Wüthrich D, C Ylla Arbós, M Pfister, AJ Schleiss (2020) "Effect of debris damming on wave-induced hydrodynamic loads against free-standing buildings with openings." Journal of Waterway, Port, Coastal, and Ocean Engineering, 146(1). https://doi.org/10.1061/(asce)ww.1943-5460.0000541

TABLES:

FIGURE CAPTION LIST:

FIGURE FILES: